Free Surface Penetration of Inverted Right Circular Cones at Low Froude Number

Samuel R. Koski

Thesis submitted to the Faculty of the
Virginia Polytechnic Institute and State University
in partial fulfillment of the requirements for the degree of

Masters of Science
in
Mechanical Engineering

Sunghwan Jung, Chair
Weiwei Deng
Jon Yagla

January 10, 2017
Blacksburg, Virginia

Keywords: boundary element method, free surface penetration, interfacial flow, water entry, Laplace's equation

Free Surface Penetration of Inverted Right Circular Cones at Low Froude Number

Samuel R. Koski

ABSTRACT

This study is focused on the impact of inverted right circular cones over multiple deadrise angles on an air water interface at low Froude number ($Fr \approx$ 10-70). In this flow regime it is known that an air cavity is formed aft of a body as it travels into a liquid. Previous studies have confirmed that the depth of the projectile at the collapse of this cavity follows a power law $\propto Fr^{1/2}$ for disks, whereas for right cylinders or the impact of spheres on soft sand, the depth at cavity seal is $\propto Fr^{1/3}$. Experiments were conducted at these Froude numbers with 0.02 m radius cones over multiple deadrise angles. High speed video was taken as well as a measurement of the drag force over the depth of travel for each case. A numerical model has been developed based on a boundary element method, and matching the conditions of the experiments, we study the temporal dynamics of the cavity and the forces exerted on the cone from impact on the liquid interface to cavity collapse.

Free Surface Penetration of Inverted Right Circular Cones at Low Froude Number

Samuel R. Koski

GENERAL AUDIENCE ABSTRACT

In this thesis the impact of inverted cones on a liquid surface is studied. It is known that with the right combination of velocity, geometry, and surface treatment, a cavity of air can be formed behind an impacting body and extended for a considerable distance. Other investigators have shown that the time and depth of the cone when this cavity collapses and seals follows a different power law for flat objects such as disks, then it does for slender objects such as cylinders. Intuitively it can be expected that a more slender body will have less drag and that the streamlined shape will not push the fluid out of it's way at impact to the same extent as a more blunt body, therefore forming a smaller cavity behind it. With a smaller initial cavity, the time and depth of it's eventual collapse can be expected to be less than that of a much more blunt object, such as a flat disk.

To study this, a numerical model has been developed to simulate cones with the same base radius but different angles impacting on a liquid surface over a range of velocities, showing how the seal depth, time at cavity seal, and drag forces change. In order to ensure the numerical model is accurate, it is compared with experimental data including high speed video and measurements made of the force with time.

It is expected that the results will fall inside the power law exponents reported by other authors for very blunt objects such as disks on one end of the spectrum, and long slender cylinders on the other. Furthermore, we expect that the drag force exerted on the cones will become lower as the L/D of the cone is increased.

ACKNOWLEDGMENTS

I'd like to thank Cathy Hill for her help, guidance, and encouragement all of these years. She was instrumental in my efforts at Virginia Tech from the start, and there is no question I would not have finished without her.

I consider myself especially privileged to have been advised by each member of my committee. It was both a deep honor and humbling experience to have had Dr. Sunghwan (Sunny) Jung as my committee chair. I'd like to thank him for sharing his experience, knowledge, and guidance, and expect it will have a lasting impact on my career and continuing education. Dr. Weiwei Deng played an important role on my committee and I thank him for taking the time to share his insight and for stepping in at such a critical time. I'd like to thank my friend and mentor of 10 years, Dr. Jon Yagla. Due to his uncanny ability to break problems down to almost any level, he has guided me through efforts ranging from basic woodworking to complex mathematics. This combined with his profound bank of knowledge and experience has unquestionably shaped me into the engineer I am today.

I'd like to thank Dr. Pavlos Vlachos for his seemingly unlimited patience and for opening up the opportunity to pursue graduate studies at Virginia Tech. His contribution to this work and my overall success are greatly appreciated.

Finally, I'd like to thank my family, especially my wife Sharon, and my children Lily and Ryan. The sacrifices you've made, particularly in the last month or two, cannot be overstated. After I've had a few months of sleep, I look forward to spending as much time as possible together.

CONTENTS

LIST OF FIGURES

LIST OF TABLES

NOMENCLATURE

Fr = Froude number

V_0 = Impact velocity

g = Standard gravity

R_0 = Radius of the cone

H_{seal} = Depth of the base of the cone below the undisturbed free surface at cavity seal

H_{exp} = Height of the cone tip above the free surface prior to release

H_z = Depth of the base of the cone below the undisturbed free surface

β = Deadrise angle

V = Velocity of the cone

R_e = Reynolds number

ν = Kinematic viscosity

ϕ = Velocity potential

δ = Dirac delta

P = Pressure

P_a = Ambient air pressure

ρ = Fluid density

γ = Interfacial tension

K = Curvature

s = Arc length

F_γ = Force contribution due to interfacial tension

F = Total drag force on the cone

$\triangle$t = Time step

R_c = Radius of the cone at the fluid contact line as the cone enters the fluid

H_t = Height of the cone tip below the undisturbed free surface

$\mathbf{n}$ = Unit normal vector

$\tilde{T}$ = Dimensionless time

$\tilde{F}$ = Dimensionless force

C_d = Drag coefficient

σ_{we} = Water entry cavitation number

α = Dimensionless acceleration

a_{avg} = Mean acceleration

1. FREE SURFACE PENETRATION OF INVERTED RIGHT CIRCULAR CONES AT LOW FROUDE NUMBER

Samuel Koski,[1] Sunghwan Jung,[2] Pavlos Vlachos,[3] Jon Yagla,[4] Austin Mituniewicz,[2] and Brian Chang[2]

[1)] *Department of Mechanical Engineering, Virginia Tech, Blacksburg, VA 24061*

[2)] *Department of Engineering Science and Mechanics, Virginia Tech, Blacksburg, VA 24061*

[3)] *Department of Mechanical Engineering, Perdue University, West Lafayette, IN 47907*

[4)] *Consultant to the Naval Surface Warfare Center - Code E41, Dahlgren, VA 22448*

In this paper, we study the impact of inverted right circular cones over multiple deadrise angles on an air water interface at low Froude number ($Fr \approx$ 10-70). In this flow regime it is known that an air cavity is formed aft of a body as it travels into a liquid. Previous studies have confirmed that the depth of the projectile at the collapse of this cavity follows a power law $\propto Fr^{1/2}$ for disks, whereas for right cylinders or the impact of spheres on soft sand, the depth at cavity seal is $\propto Fr^{1/3}$. Experiments were conducted at these Froude numbers with 0.02 m radius cones over multiple deadrise angles. High speed video was taken as well as a measurement of the drag force over the depth of travel for each case. A numerical model has been developed based on a boundary element method, and matching the conditions of the experiments, we study the temporal dynamics of the cavity and the forces exerted on the cone from impact on the liquid interface to cavity collapse.

PACS numbers: 02.60.Lj, 02.60.-x, 47.11.-j, 47.55.N-+

1.1. Introduction

Free surface penetration is a multiphase flow phenomenon whereby a solid body is translated through a gas penetrating a liquid. Divers or seaplane floats impacting a fluid surface[2,3], plunge-diving seabirds[4], and water striders[5] or basilisk lizards[6] running on water include examples in this class of problem. Classical work by Worthington[7] showed that for a given surface treatment, body geometry, and impact velocity a "basket splash" and transient cavity can be maintained as a sphere travels from air into fluids such as water, petroleum, and glycerin.

For projectiles with sharp corners such as disks and cones, the point at which the fluid separates from the body at impact is well defined and much less dependent on the surface treatment. Glasheen and McMahon[1] performed an experimental study with disks ranging in radius from 0.01-0.03 m and Froude numbers $Fr = {V_0}^2/gR_0$ from 1-80, where V_0 is the initial velocity, R_0 the radius, and g is the acceleration due to gravity. Accounting for hydrostatic pressure, a projectile weight which matched the average drag force enabled experimentation conducted with a steady average velocity, providing for a more direct comparison with steady-state numerical and experimental results. From this, it was shown that the non-dimensional depth at seal was related to the square-root of the Froude number as $H_{seal}/R_0 = 2.30Fr^{0.5}$. They also found that the time to seal was nearly independent of velocity, and related to the square root of the radius as $0.73{R_0}^{0.5}$.

Multiple investigators have since confirmed these findings numerically and experimentally[8–10]. Experimentation and modeling conducted by Lohse *et al.*[11] included the impact of spheres on extremely fine aerated sand, where the depth at seal was found instead to be $\propto Fr^{1/3}$. This work was extended by Duclaux *et al.*[10] where experimentation and analytical modeling was conducted confirming both of these power laws, with the depth at seal for spheres $\propto Fr^{1/2}$ and cylinders $\propto Fr^{1/3}$.

In this article, we investigate the effect that cone deadrise angle has on the cavity interface dynamics, including pinch off time and depth, interface position, and the drag force on the cone at low Froude number ($Fr \approx 10 - 70$). We set out to show that as a result of the differing angles, the seal depth falls inside the range $\propto Fr^{1/n}$ where $2 < n < 3$. To carry this out, assumptions must be made about the relative importance of governing parameters. At the impact velocities under consideration, the dynamic pressures that initially push the

fluid radially outward are quickly overcome and dominated by hydrostatic pressure as the cavity wall behind the cone is extended and begins to collapse. As a result, forces due to gravity and interfacial tension have a marked effect on the cavity development and cannot be neglected. This was shown by Gaudet[9] to be particularly important at very low Froude number, where the fluid initially has minimal outward motion at impact and begins to collapse almost immediately thereafter.

With these considerations in mind, we develop a boundary element scheme similar to Oguz and Prosperetti[12] and Gaudet[9] which numerically simulates the evolution of the cavity in time. The results of controlled experiments, including measurements of force, are then compared and expanded with this model to gain insight into the cavity dynamics.

In §II we will discuss the experimental setup, and the mathematical formulation is covered in §III followed by the numerical method in §IV. A comparison will then be made in §V between the experimental and numerical results, including the position of the interface, time and depth at cavity seal, and the drag force exerted on the surface of the cone. Finally, we discuss the results and draw conclusions and recommendations in §VI.

1.2. Experimental set-up

Experiments have been conducted with 0.02 m fixed radius (R_0) cones at deadrise angles (β) of 45, 60, and 77.5 degrees. A sketch of the experimental setup is provided as Fig. 1. The supporting structure around the water tank was constructed of aluminum t-slot beams. Low friction sliding supports were mounted onto each of the vertical beams and onto each of these an end of the horizontal cross member was secured. Force measurements were made using an Omegadyne LCM105-10 load cell securely mounted at the center of the cross member. The data was collected at 1000 samples/second with a National Instruments DAQ after passing though a signal amplifier. A 3.18 mm radius stainless steel rod was threaded into the load cell on one end and into a cone on the other. Experiments were conducted with the tip of the cone located at a height H_{exp}=10-60 cm above the surface of the water. This was achieved by securing a line to the sliding cross bar assembly and lifting it into place by means of a pulley. Upon release, the cone was free to fall vertically to the fluid interface, impacting at an instantaneous velocity $V_0 \approx \sqrt{2gH_{exp}}$. Unlike the steady experiments of Glasheen and McMahon[1], and the decelerating cases studied by Duclaux *et al.*[10], the cones

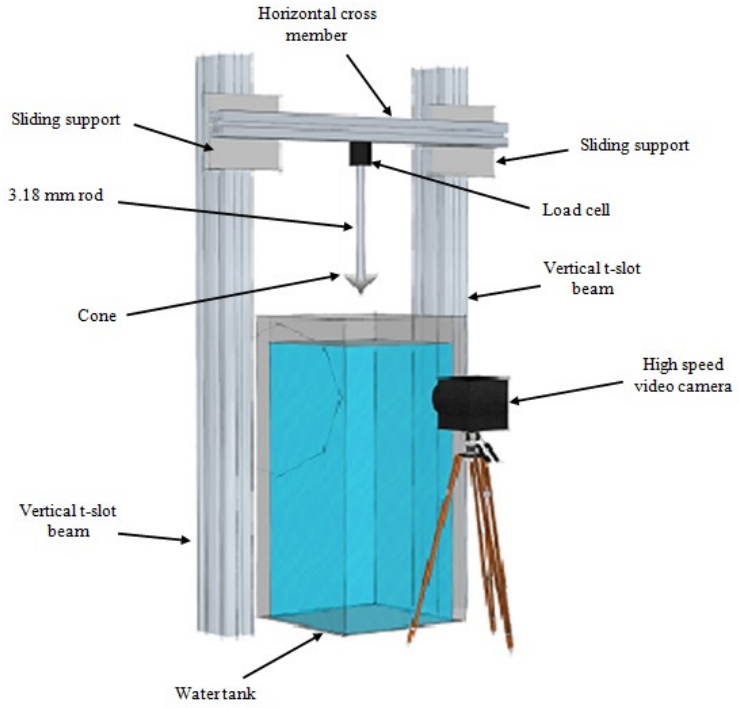

Figure 1: Experimental set-up.

for these experiments continue to accelerate an average of 2-5 m/s^2 from impact to cavity seal ($\approx$ 0.1 s). Shadowgraphs were taken with a high speed IDT Motionxtra N3 camera at 1000 frames per second with a shutter speed of 63 μs. The images were captured at a resolution of 408$\times$1248 pixels. The cone impacted the fluid interface at the center of the tank, so that the camera captured the event as the cone crossed the fluid air interface from below the surface. Although this recorded the temporal cavity dynamics below the free surface well, the effects that occurred above it could not be recorded since, when looking at the interface from inside the fluid, light was reflected off the air water interface.

1.3. Mathematical formulation

We set out to calculate the transient cavity dynamics encompassing the configuration and conditions of the experiments. The axisymmetric region displayed in Fig. 2 defines the coordinate system and domain. A cone with a deadrise angle β impacts the fluid interface vertically along the z axis with a velocity $V(t)$. The bottom and far field boundaries are

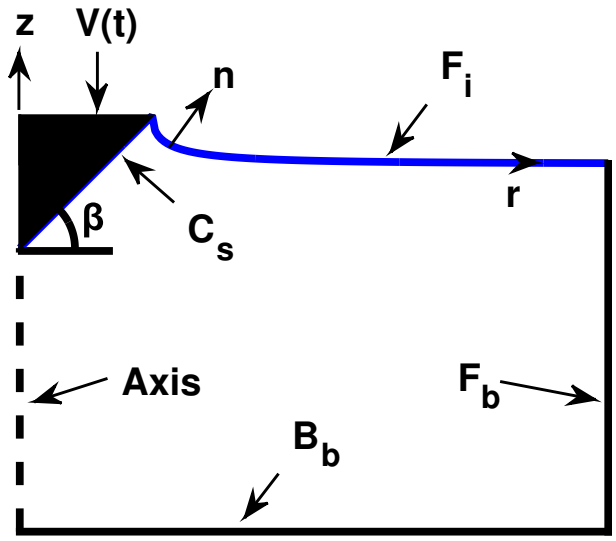

Figure 2: Axisymmetric domain definitions.

positioned sufficiently far away that they have a negligible influence on the flow. At the impact velocities under evaluation, the Reynolds number $R_e = R_0 V_0/\nu$ is on the order 10^4 or higher, so that the fluid is considered both inviscid and incompressible. It is assumed also that the flow is irrotational, which means a velocity potential ϕ(r,z,t) exists inside the fluid volume satisfying Laplace's equation

$$\bigtriangledown^2 \phi = 0. \tag{1}$$

Since our interest lies exclusively on the dynamics occurring on the boundary, a boundary integral method is ideally suited for the problem. To carry this out, we employ the Green's function of Laplace's equation given by

$$\bigtriangledown^2 G(\mathbf{x}, \mathbf{x}_0) + \delta(\mathbf{x} - \mathbf{x}_0) = 0, \tag{2}$$

where

$$|\mathbf{x} - \mathbf{x}_0| = \sqrt{(x - x_0)^2 + (y - y_0)^2 + (z - z_0)^2} \tag{3}$$

is the distance of a field point $\mathbf{x}$ from the singular or source point $\mathbf{x}_0$. The fundamental solution of Laplace's equation in the absence of boundaries is known to be[13]

$$G(\mathbf{x}, \mathbf{x}_0) = \frac{1}{4\pi|\mathbf{x} - \mathbf{x}_0|}. \tag{4}$$

Referring to Fig. 2, we see that the solution domain of interest is rotationally symmetric about the z axis and thus integrate Eq. 4 from 0 to 2π, which yields

$$G\left(\boldsymbol{\xi},\boldsymbol{\xi}_0\right)=\frac{F(k)}{\pi\sqrt{\left(z-z_0\right)^2-\left(r+r_0\right)^2}}, \tag{5}$$

representing the value of a function at $\boldsymbol{\xi}$ due to a point source at $\boldsymbol{\xi}_0$ in an infinite domain. Here, $F(k)$ is the complete elliptic integral of the first kind

$$F(k)=\int_1^{2\pi}\frac{d\eta}{\sqrt{1-k^2\cos^2\eta}}, \tag{6}$$

where η is a dummy variable of integration and

$$k^2=\frac{4rr_0}{(z-z_0)^2+(r+r_0)^2}. \tag{7}$$

For a bounded domain, we find after substitution of Eq. 2 into Green's second identity, an integral equation for the solution of Laplace's equation by integrating over a control volume $\mathcal{V}$ bounded by a surface $S=C_s\cup F_i\cup F_b\cup B_b$ to be

$$\int_S -G\left(\boldsymbol{\xi},\boldsymbol{\xi}_0\right)\mathbf{n}\cdot\bigtriangledown\phi\left(\boldsymbol{\xi}\right)+\phi\left(\boldsymbol{\xi}\right)\mathbf{n}\cdot\bigtriangledown G\left(\boldsymbol{\xi},\boldsymbol{\xi}_0\right)ds=\lambda\phi\left(\boldsymbol{\xi}_0\right), \tag{8}$$

where s is the arc length along S. Integration of $\delta(\mathbf{x}-\mathbf{x}_0)$ is by definition a Heaviside function from which

$$\lambda=\begin{cases}1 & \text{if } \boldsymbol{\xi}_0 \text{ lies inside } \mathcal{V}\\ 1/2 & \text{if } \boldsymbol{\xi}_0 \text{ lies on S}\\ 0 & \text{if } \boldsymbol{\xi}_0 \text{ lies outside } \mathcal{V}\end{cases}. \tag{9}$$

The unsteady Bernoulli equation given by

$$P-P_a=-\rho\left(gH_z+\frac{\partial\phi}{\partial t}+\frac{1}{2}|\bigtriangledown\phi|^2\right), \tag{10}$$

provides a means by which the pressure (P) inside the fluid volume can be determined, where P_a is the ambient air pressure, H_z is the depth from the base of the cone to the undisturbed free surface, and ρ is the fluid density. Recalling that the Young-Laplace equation $\triangle P=\gamma K$ relates the pressure difference across the fluid interface (F_i) to the mean curvature and interfacial tension, we recast Eq. 10 to find the Lagrangian time rate of change of the velocity potential as

$$\left.\frac{\partial\phi}{\partial t}\right|_{F_i}=\frac{1}{2}|\bigtriangledown\phi|^2-gH_z-\frac{\gamma K}{\rho}, \tag{11}$$

where γ is the interfacial tension and the mean curvature

$$K = \frac{\dot{z}\ddot{r} - \dot{r}\ddot{z}}{\left(\dot{r}^2 + \dot{z}^2\right)^{3/2}} - \frac{\dot{z}}{r\left(\dot{r}^2 + \dot{z}^2\right)^{1/2}} \tag{12}$$

with the dots denoting differentiation with respect to arc length.
For the calculation of drag, the force contribution due to interfacial tension acting at the edge of the cone is determined to be

$$F_\gamma = 2\pi R_0 \gamma \cos\left(\theta\right), \tag{13}$$

where θ is the angle of the interface from the z axis on the edge of the cone located at R_0. The fluid pressure acting at the wetted cone surface is found by integration of Eq. 10 in polar coordinates from r=0 to R_0, so that the total drag force is given by

$$F = A_c \rho \left(\frac{1}{2} {V_n}^2 - \beta \int_{r=0}^{R_0} \left(\frac{\partial \phi}{\partial t} - \frac{1}{2} \left(\frac{\partial \phi}{\partial s} \right)^2 - g H_z \right) r dr \right) + 2\pi R_0 \gamma \cos\left(\theta\right), \tag{14}$$

where A_c is the wetted area of the cone, and $\partial\phi/\partial s$ is the tangential velocity of the fluid at the cone surface. Recalling that the unknown velocity potential on the cone surface is calculated in time by Eq. 8, the definition of a material derivative can be used to find

$$\frac{\partial \phi}{\partial t} = \frac{D\phi}{Dt} - \mathbf{V}(t) \cdot \bigtriangledown \phi \tag{15}$$

assuming $D\phi/Dt \cong \triangle\phi/\triangle t$.

1.4. Numerical method

1.4.1. Boundary element method (BEM)

In order to solve Eq. 8 numerically, the boundary S is approximated by nodes (z_1, r_1),(z_2, r_2) $\ldots\ldots$ (z_{N+1}, r_{N+1}), joined by straight line elements E_k with $k = 1, 2, \ldots, N$. Assuming constant $\phi = \phi_k$ and $\partial\phi/\partial n = V_k$ at the center of each element Eq. 8 can be written

$$\lambda\phi(z_0, r_0) = \sum_{k=1}^{N} -\alpha_k(z_0, r_0) V_k + \phi_k \psi_k(z_0, r_0), \tag{16}$$

where

$$\alpha_k(z_0, r_0) = \int_{E_k} G\left(\boldsymbol{\xi}, \boldsymbol{\xi}_0\right) ds \tag{17}$$

and

$$\psi_k(z_0, r_0) = \int_{E_k} \mathbf{n} \cdot \bigtriangledown G\left(\boldsymbol{\xi}, \boldsymbol{\xi}_0\right) ds. \tag{18}$$

Recalling that our interest lies only on the boundary, we set $\lambda = 1/2$ so that Eq. 16 can be written

$$\frac{1}{2}\phi_j = \sum_{k=1}^{N} \phi_k \psi_{jk} - V_k \alpha_{jk}, \tag{19}$$

where the index j represents the evaluation node (z_0, r_0) on a boundary element. In order to solve Eq. 19 numerically we write it in the form $\mathbf{Ax}$=$\mathbf{b}$, where the known values are stored in the matrix $\mathbf{A}$ and vector $\mathbf{b}$ in order to calculate the unknown values represented by the vector $\mathbf{x}$

$$\sum_{k=1}^{N} A_{jk} x_k = \sum_{k=1}^{N} b_{jk}. \tag{20}$$

To construct the $\mathbf{A}$ matrix and $\mathbf{b}$ vector, the line integrals for Eq. 17 and 18 are computed with a 20 point Gaussian quadrature. For our problem either ϕ_k is known on the fluid interface or V_k is known on the surface of the cone in Eq. 19. So that on an element where ϕ_k is known and V_k is unknown, $A_{jk} = -\alpha_k(z_k, r_k)$ and $b_{jk} = -\phi_k \psi_k(z_k, r_k)$ if $j \neq k$ and $b_{jk} = -\phi_k \psi_k(z_k, r_k) + 1/2\phi_j$ if $j = k$. Alternately when V_k is known and ϕ_k is unknown, $A_{jk} = \psi_k(z_k, r_k)$ if $j \neq k$ or $\psi_k(z_k, r_k) - 1/2$ if $j = k$, and $b_{jk} = V_k \alpha_k(z_k, r_k)$.

1.4.2. Initial conditions

We start our calculation with the cone surface fully wetted, where the initial shape of the free surface and depth of the cone are determined by Wagner's method[2]. The depth of the cone tip below the undisturbed free surface H_t is first found by[14]

$$H_t = \frac{\pi R_c \tan\beta}{4}, \tag{21}$$

where R_c is the radius of the cone at the fluid contact line. Setting $R_c = R_0$, the fully submerged depth is determined and the initial interface profile is calculated by[15]

$$\zeta(r, t_0) = \frac{r H_t}{R_0} \arcsin\left(\frac{R_0}{r}\right) - H_t, \qquad for\ r > R_0. \tag{22}$$

Experiments were conducted for cones with deadrise angles of 45, 60 and 77.5 degrees dropped from 10-60 cm heights in increments of 10 cm. For each drop height 5 experiments were conducted with high speed video taken as well as measurements made of the drag force exerted on the cone. The mean of the velocity was taken of all 5 samples for a given drop height, and a quadratic fit of this was used as input into the numerical code for $V(t)$. In order to make a quantitative comparison of the experimental and numerical cases, post processing of the high speed video data was carried out using the image processing toolbox available in the technical computing software MATLAB[16,17]. Each of the video frames were saved as .tiff files, which could be directly read into MATLAB. Once loaded, an image was converted to binary using the im2bw function, as shown in Fig. 3. The result of this was an image where the region at the cavity interface was represented by ones (white) and the remaining pixels were given a value of zero (black). With the image converted to binary, extraction of the interface was carried out using the bwtraceboundary function. Prior to a series of experiments, an image was taken with the high speed camera of a ruler, allowing for scaling of the extracted interface from pixels to a spatial unit. Due to the fact that our simulations start with the cone fully submerged, the correct start time is determined from the experimental data by fitting a curve to the average cone depth with time. Differentiation of this provides an equation for $V(t)$, and the time at H_t is then used as input into this equation to determine the initial velocity for the calculation. At this time the velocity potential is set to $\phi = 0$ on the fluid interface, and the velocity $\partial\phi/\partial n = \mathbf{V}_0 \cdot \mathbf{n}$ at the cone surface, where $\mathbf{n}$ is the unit normal pointing out of the fluid volume.

Adequate nodal spacing is important for proper resolution of the interface, particularly in the early stages of the solution when the position of the fluid interface is rapidly evolving. The arc length spacing of the nodes ($\triangle$s) is set at the beginning of the simulation and held constant until its completion. We have found it to be important that the same arc length spacing on both the cone surface and interface also be maintained throughout the calculation[18] ($\triangle s/R_0$=0.02). However, the far field boundaries have little effect on the flow, and hence are sparsely populated with nodes, which has the added benefit of reducing computational expense.

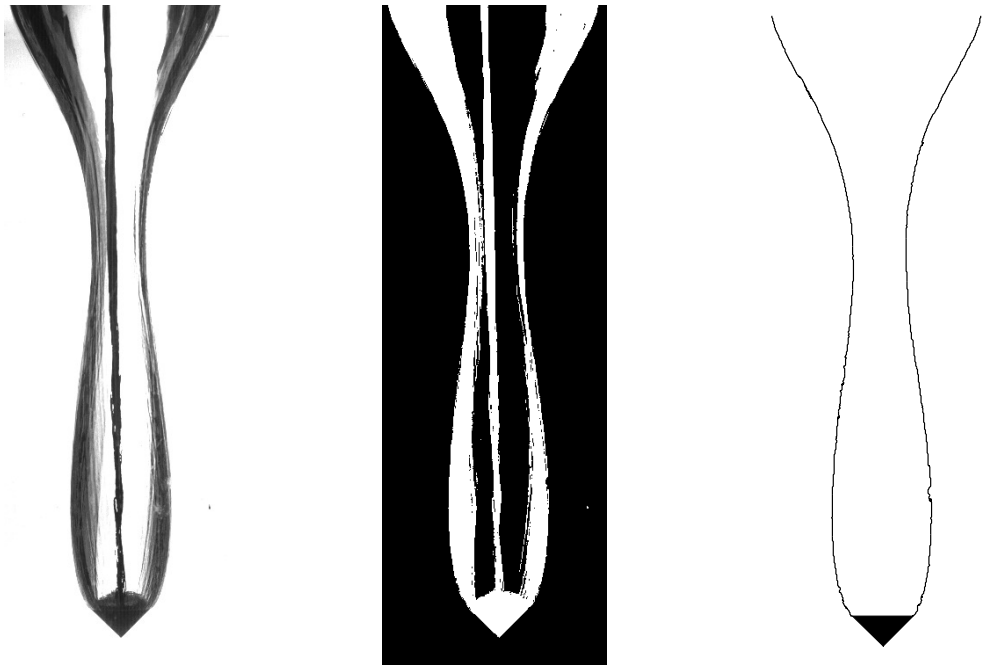

(a) (b) (c)

Figure 3: Image processing sequence where (a) is the raw image from the high speed video, (b) is the image converted to binary, and (c) is fluid interface after extraction.

1.4.3. Time integration

Fig. 4 is included to illustrate the general process used to carry out a numerical simulation. By means of Eq. 20, we use the initial conditions on the boundary to find the unknown velocity potential at the cone surface and the normal velocity on the fluid interface at the center of each element. To advance the solution in time, the position of the cone is determined by $V(t)\Delta t$. The advancement of the interface, and the calculation of Eq. 11 are carried out by means of a 4th order Runge-Kutta method.

At each iteration, the position of the nodes are changed by some spatial distance depending on the local fluid velocity and time step. As a result, it is necessary to add and redistribute nodes as the solution advances to ensure the interface is properly resolved. Although the nodal spacing is maintained throughout the calculation, the first node on the interface next to the cone is alternately placed at arc length $\triangle s$ and $1/2\ \triangle s$ every time step, following the

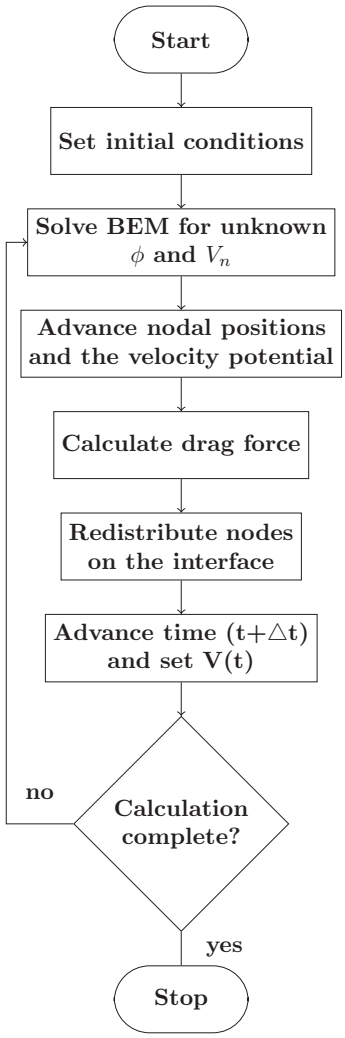

Figure 4: Steps for numerical solution.

work of Oguz and Prosperetti[12]. This has the advantage of smoothing the interface while preventing the growth of artificial instabilities.

The fluid interface is represented by parametric splines in order to determine the nodal positions and velocity potential during the redistribution process. Oguz and Prosperetti[12], Gaudet[9], and Dommermuth and Yue[19] all represented the fluid interface by parametric cubic splines. In regions of evolving curvature, such as where the fluid heaves upward near the cone edge at initial impact and where deep seal occurs, standard cubic splines often impose an exaggerated curvature on the interface, the extent of which is a function of nodal resolution and the local curvature. Besides effecting the estimation of the interface position with time, the presence of irregularities on the fluid interface introduce numerical noise when differentiating with respect to arc length. To counter this, we use the monotone piece-wise

cubic by Fritsch and Carlson[20] who suggested that unlike other spline types, "*the curve produced contains no extraneous bumps or wiggles, which makes it more readily acceptable to scientists and engineers.*"

1.5. Experimental and numerical results

In this section we make a comparison between the results of our numerical simulations and experiments, including the position of the interface, time and depth at cavity seal, and the drag force exerted on the surface of the cone.

1.5.1. Dynamics of the fluid interface

Fig. 5 shows results for a selection of the 60 cm drop height experiments, where the numerically calculated interface position is overlaid on images for each of the cone deadrise angles at dimensionless times H_z/R_0=5, H_z/R_0=10, and just prior to cavity seal. It can be seen from this that upon impact on the air water interface, the water is accelerated radially outward from the edge of the cone. This produces an air cavity aft of the cone with a radius that is a function of the cone angle and impact velocity. As the cone moves further into the fluid, the wall of the cavity becomes less affected by the cone, and hydrostatic pressure begins to push it radially inward. The differences in cavity development for each of the cones is clearly seen by this, where the higher deadrise angle cones are less able to push the fluid radially outward and hence produce a cavity which has less volume. The numerical results match the location of the interface in time very nicely for these cases. However, near the fluid free surface there is some localized difference due to the splash, which is not accounted for numerically. This clearly has little effect on the overall development of the cavity interface. The error associated with this becomes larger with drop height and lower cone deadrise angle, so that the images shown in column c of Fig. 5 represent the worst case out of all the experiments conducted.

Considering the cases shown in images at cavity seal in Fig. 5, it is clear that the time of complete cavity closure and hence the depth of the cone at pinching was not directly measurable due to the presence of the rod pushing the cone into the fluid. Using the interface position extracted from the high speed video, we were able to track the minimum

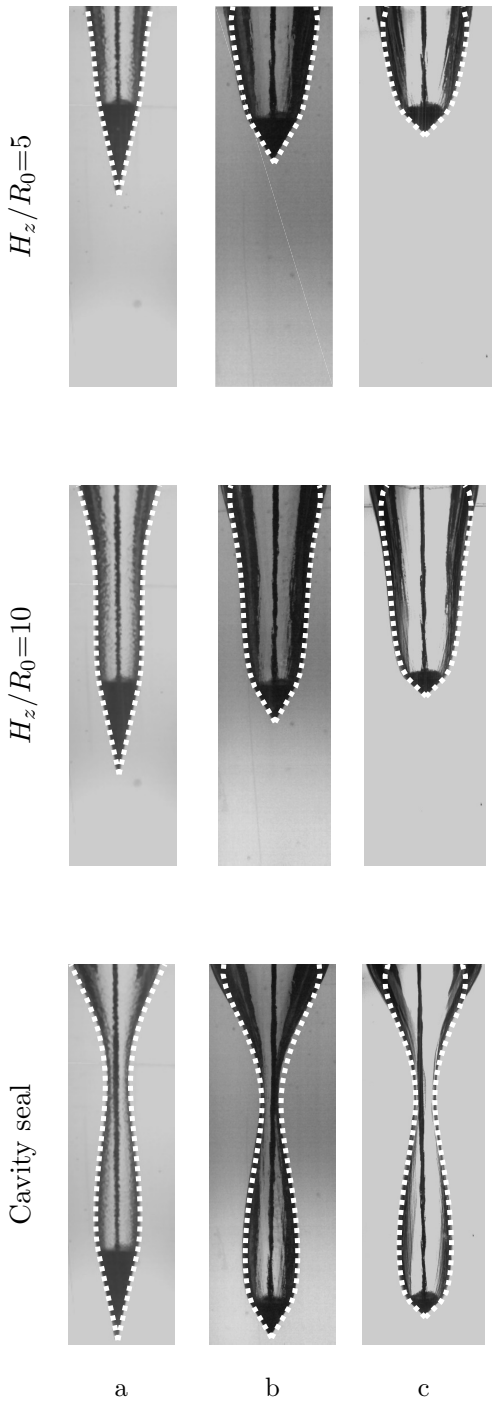

Figure 5: Cavity development for the 77.5^o cone (column a), 60^o cone (column b), and 45^o cone (column c) dropped from H_{exp}=60 cm. The cones are shown at depths H_z/R_0=5, H_z/R_0=10, and just prior to cavity seal, where H_z/R_0=20.72 for the 45^o cone, H_z/R_0=18 for the 60^o cone, and H_z/R_0=14.66 for the 77.5^o cone.

radius of the cavity in time as the interface began to close in on itself. A curve fit and extrapolation of this data enabled a reasonable estimation of the seal depth and time for comparison with the numerical results.

1.5.2. Depth and time at cavity seal

The depth at which cavity seal occurs is taken as the distance from the base of the cone to the undisturbed fluid free surface. Fig. 6a shows the comparison between the experimental and numerical results for dimensionless seal depth H_z/R_0. Since we match the velocity

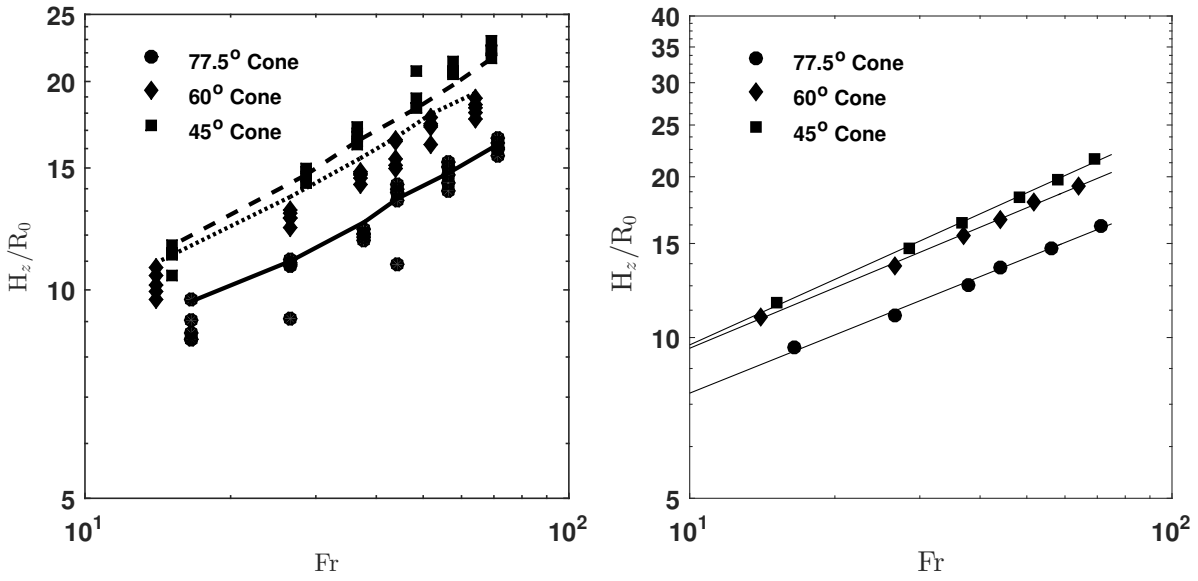

Figure 6: (a) Comparison between numerical and experimental dimensionless seal depth for R_0=0.018 m cones. For the numerical cases the 77.5^o cone is represented by the solid line, the 60^o cone is the dotted line, and the 45^o cone the dashed line. (b) Numerical dimensionless seal depth (H_z/R_0) for cones with deadrise angles of 77.5, 60, and 45 degrees matching the experimental conditions. The power law fit for the 45^o cone is $H_z/R_0 = 3.79Fr^{0.41}$, the 60^o cone is $H_z/R_0 = 4.01Fr^{0.38}$, and the 77.5^o cone is $H_z/R_0 = 3.42Fr^{0.36}$.

profile of the experimental cases, the numerical results do not follow the expected smooth trend. However, although the 60^o cone case seems to slightly over predict the experimental

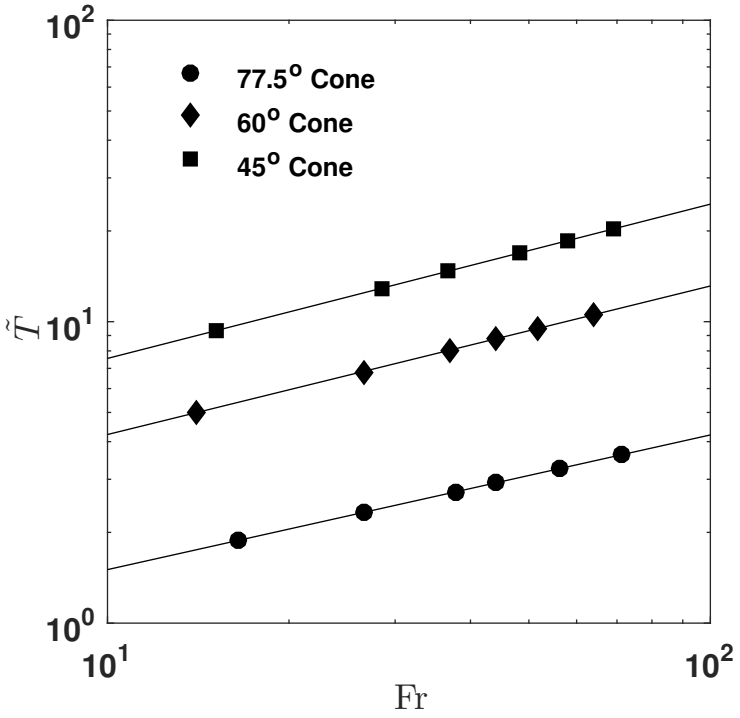

Figure 7: Comparison between numerical (solid line) and experimental (∘) dimensionless time to seal ($\tilde{T}$) for R_0=0.02 m cones with deadrise angles of 77.5, 60, and 45 degrees and Froude numbers ($Fr = V_0^2/gR_0$) ranging from ≈10-70.

data, the comparison between the numerical and experimental results are quite good. In Fig. 6b a plot of the numerical data corresponding to the experimental cases with power law fits is included. Here we see that for the 45^o cone $H_z/R_0 = 3.79Fr^{0.41}$, the 60^o cone $H_z/R_0 = 4.01Fr^{0.38}$, and the 77.5^o cone $H_z/R_0 = 3.42Fr^{0.36}$. Which confirms that as the deadrise angle and hence the L/D is decreased for a fixed radius cone (e.g. it becomes more blunt), the fluid has a greater radial momentum at the separation point, and hence the interface dynamics approach that of the disks studied by Glasheen and McMahon[1] and Gaudet[9], where the depth at seal was $\propto Fr^{0.5}$. Conversely, as the deadrise angle is increased, the fluid experiences less radial motion at the edge of the cone and hence the cavity wall is more quickly overcome by hydrostatic pressure, thereby producing a more rapid cavity closure.

This is verified by the corresponding time to seal, normalized by $\tilde{T} = t/(H_{cone}/V_0)$ shown in Fig. 7 for each of the cones. As expected, the magnitude of $\tilde{T}$ increases with cone angle, however it is notable that, unlike the seal depth, the dimensionless time to seal is

approximated by a power law fit $\propto Fr^{0.5}$ regardless of cone angle.

1.5.3. Drag force

Measurements of drag force were made for each of the experiments conducted, and corresponding numerical runs were completed matching the conditions of each. Fig. 8 includes a plot of drag force normalized by $\tilde{F} = F/(\frac{\pi}{2}\rho R_0^2 V_0^2 \cot\beta)$ with dimensionless time $\tilde{T}$, where H_{cone} is the cone height. For all of the cases, the force is increasing as the cone is driven into

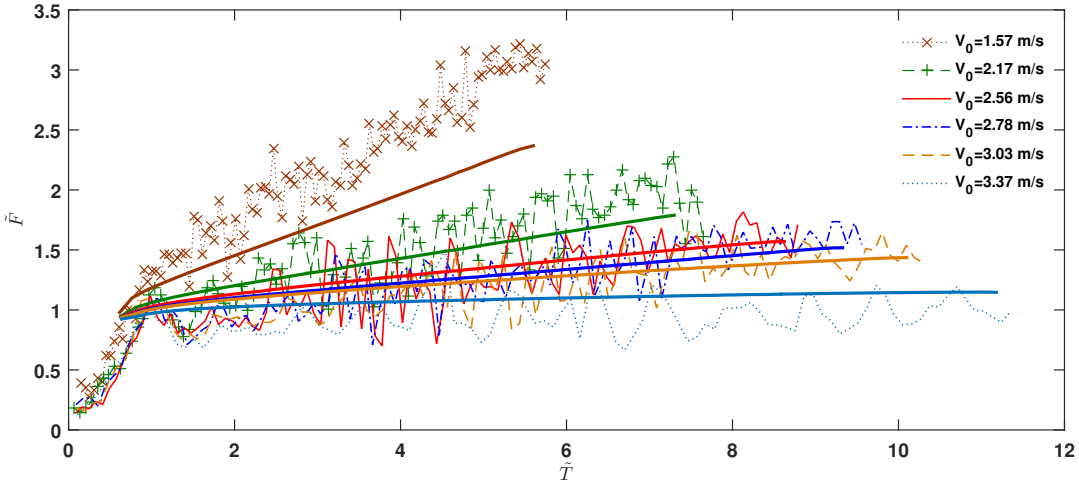

Figure 8: Comparison of normalized force $\tilde{F} = F/(\frac{\pi}{2}\rho R_0^2 V_0^2 \cot\beta)$ with time $\tilde{T} = t/(H_{cone}/V_0)$ for all experimental cases and numerical runs for the 60^o deadrise angle cone. The numerical data is represented by the smooth lines, colored to match the corresponding experimental data

the fluid, a result of both the increasing hydrostatic pressure with depth and velocity with time. The numerical method slightly underestimates the force for most of the cases, with an increasing error as the impact velocity decreases. This is not unexpected, due to the fact that viscosity is not accounted for in the code. Table 1 includes the RMS error (RMSE) between the numerical and experimental data for all of the cone deadrise angles and drop heights. For nearly all of the cases, the the RMSE falls in the range 0.15 to 0.5. From the numerically calculated force we obtain the coefficient of drag for the cones (C_d) by

$$C_d = \frac{F(t)}{0.5\rho V^2 \pi R_0^2}. \tag{23}$$

TABLE 1: Numerical vs experimental RMSE

H_{exp}(cm)	RMS error 77.5^o cone	RMS error 60^o cone	RMS error 45^o cone
10	1.20	0.51	0.55
20	0.67	0.23	0.41
30	0.48	0.21	0.5
40	0.41	0.18	0.39
50	0.54	0.17	0.44
60	0.78	0.21	0.39

Glasheen and McMahon[1] related this to the water entry cavitation number given by

$$\sigma_{we} = \frac{g|H_z(t)|}{0.5V(t)^2}, \tag{24}$$

which by taking into account the changing depth and velocity with time, is a ratio between hydrostatic and dynamic pressure. In their work, they found a linear relationship between the two which was later confirmed by Gaudet[9]. Since they were interested in studying disks with a near constant velocity, they only reported data that had dimensionless acceleration (α) less than 0.015 given as

$$\alpha = \frac{a_{avg}R_0}{V_{rms}^2}, \tag{25}$$

where a_{avg} is the mean acceleration. For our cones, α ranges from $\approx 5\times10^{-3}$ for the highest impact velocity cases to $\approx$0.03 for the lowest. Despite this we also see a linear relationship for all of the cone angles and drop heights studied as shown in Fig. 9. In this case, the slope of the line through a set of data decreases as the deadrise angle is increased, so that for the 77.5 degree cone C_d is decreasing with σ_{we} and the 45 degree cone is increasing. It is therefore reasonable to assume that as the deadrise angle continues to decrease the slope will continue to increase, approaching the plotted data from Glasheen and McMahon[1] for a disk. We also note that not unexpectedly the magnitude of C_d decreases with an increasing L/D.

For any of the cone angles, the corresponding change in drag coefficient with Froude number for a given α over the range of velocities studied is not significant. A closer view

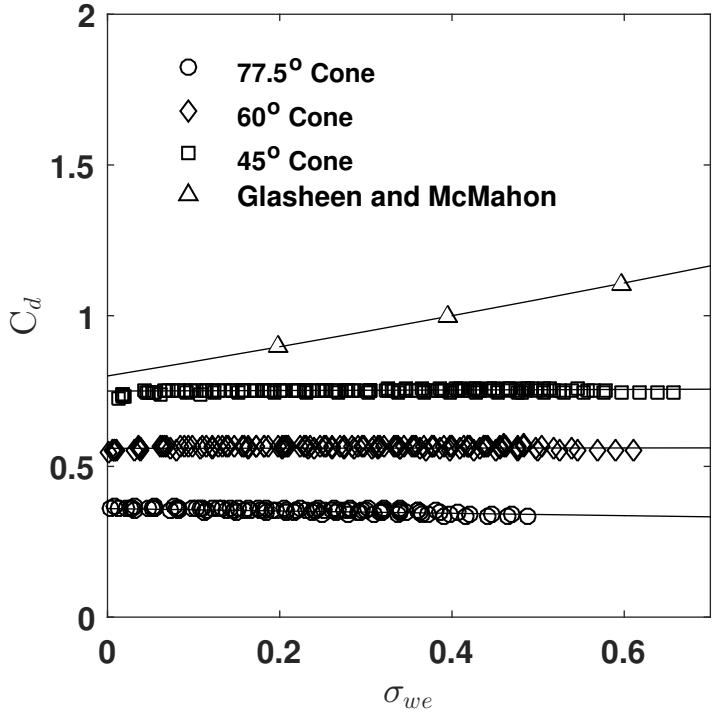

Figure 9: C_d plotted against σ_{we} for all of the cones and Froude numbers, as well as the approximate data for a disk from Glasheen and McMahon[1]

of the data illustrated in Fig. 9 is shown in Fig. 10, where all of the 77.5^o cone cases are plotted. As expected, we see an increasing C_d with V_0. However, since the velocity range is quite small, the change in C_d is not significant.

1.6. Conclusions

We have presented a quantitative numerical and experimental analysis of the temporal interface dynamics and drag force on the surface of a cone, from its impact on a liquid surface to the eventual collapse of the ensuing air cavity. Our numerical technique, based on a boundary element method, has been shown to match the experimental time to cavity seal, drag force, cavity seal depth, and interface position with excellent precision. We attribute this accuracy in part due to the representation of the interface by a parametric monotone piece-wise cubic[20], rather than the cubic splines typically used. This is coupled with a uniform fixed arc-length spacing of the nodes across the surface of both the projectile body

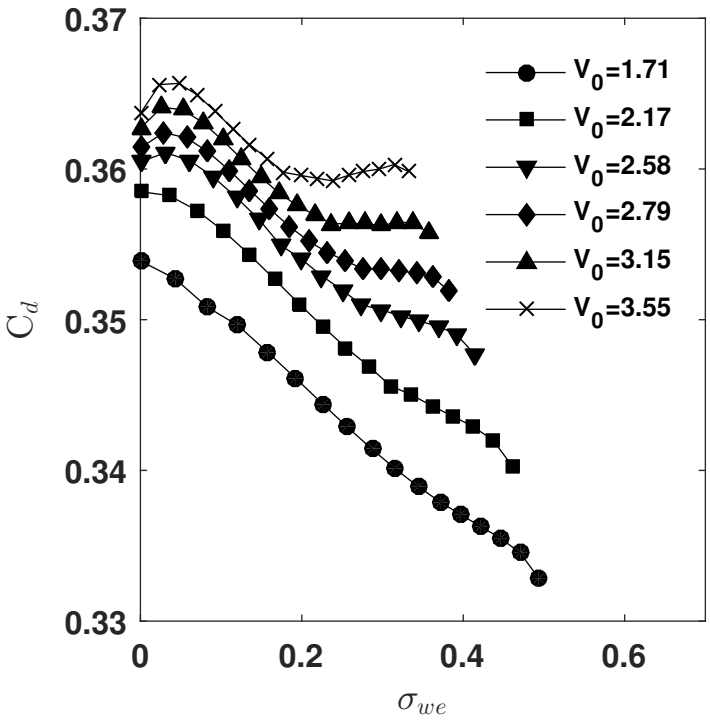

Figure 10: 77.5^o cone drag coefficient with water entry cavitation number (σ_{we}) for all Froude numbers corresponding to the cone drop heights of 10-60 cm used in the experiments.

and the interface for the entire simulation.

We confirm a linear relationship between the drag coefficient C_d and the water entry cavitation number σ_{we}, where the slope increases with decreasing deadrise angle, approaching that of the disks studied by Glasheen and McMahon[1]. The numerical method slightly under predicts the force for all of the cases. This is not unexpected, since when formulating the numerical method, we assume the flow to be inviscid and hence make no account for the boundary layer on the surface of the cone.

It has been shown that the seal depth for a cone is controlled by deadrise angle, falling inside the range $\propto Fr^{1/n}$ where $2 \leq n \leq 3$. More specifically, cones with a lower deadrise angle approach the seal depth of disks[1] or hydrophobic spheres[10], whereas more slender cones with higher deadrise angle have a seal depth approaching right cylinders[10] or spheres impacting on fine sand[11]. Similarly, the dimensionless time to seal $\tilde{T} = t/(H_{cone}/V_0)$ increases as cone angle is decreased. However, unlike the seal depth, the time to seal has been shown to be approximately $\propto Fr^{0.5}$, regardless of cone angle.

1.6.1. Future work

The study presented here focuses solely on the dynamics of the cavity interface behind a water-entering cone. It would be instructive to also consider the dynamics of bulk fluid flows, particularly along the surface of the cone and in the vicinity of the cavity interface. The boundary element code developed for this work can be extended to this effort, and a direct comparison with a technique such as particle image velocimetry (PIV) could be useful to verify the code.

A greater expansion of the numerically modeled cases would also be particularly useful. The focus of this work was on matching the cavity shape observed in the experiments, but it would be interesting to show a larger range of cone angles and velocities. Furthermore, although the acceleration was small, a comparison with these results and those of steady velocity cones or those with mass could be a follow on to this effort.

1.7. REFERENCES

[1]J. W. Glasheen and T. A. McMahon, "Vertical water entry of disks at low froude numbers," Physics of Fluids **8** (1996).

[2]H. Wagner, "Phenomena associated with impacts and sliding on liquid surfaces," Z. Angew. Math. Mech. **12** (1932).

[3]T. V. Karman, "The impact on seaplane floats during landing," National Advisory Committee for Aeronautics (1929), technical Note No. 321.

[4]M. Croson, L. Straker, S. Gart, C. Dove, J. Gerwin, and S. Jung, "How seabirds plunge-dive without injuries," PNAS **113** (2016).

[5]D. L. Hu, B. Chan, and J. W. M. Bush, "The hydrodynamics of water strider locomotion," Nature **424**, 663–666 (2003).

[6]J. W. Glasheen and T. A. McMahon, "A hydrodynamic model of locomotion in the basilisk lizard," Nature **380**, 340–342 (1996).

[7]A. M. Worthington, "A study of splashes," Longmans Green and Company (1908).

[8]R. Bergmann, D. VD Meer, S. Gekle, A. VD Bos, and D. Lohse, "Controlled impact of a disk on a water surface: cavity dynamics," J. Fluid Mech. **633**, 381–409 (2009).

[9]S. Gaudet, "Numerical simulation of circular disks entering the free surface of a fluid," Physics of Fluids **10** (1998).

[10]V. Duclaux, F. Caille, C. Duez, C. Ybert, L. Bocquet, and C. Clanet, "Dynamics of transient cavities," J. Fluid Mech. **591** (2007).

[11]D. Lohse, R. Bergmann, R. Mikkelsen, C. Zeilstra, D. VD Meer, M. Versluis, K. VD Weele, M. VD Hoef, and H. Kuipers, "Impact on soft sand: void collapse and jet formation," Physical Review Letters **93** (2004).

[12]H. N. Oguz and A. Prosperetti, "Bubble entrainment by the impact of drops on liquid surfaces," J. Fluid Mech **219**, 143–179 (1990).

[13]C. Pozrikidis, *A Practical Guide to Boundary Element Methods* (Chapman & Hall/CRC, 2000 N.W. Corporate Blvd, Boca Raton, FL 33431, 2002).

[14]O. Faltinsen and R. Zhao, "Water entry of ship sections and axisymmetric bodies," AGARD FDP and Ukraine institute of hydromechanics workshop on highSpeed body motion in water (1971).

[15]H. Sun, *A Boundary Element Method Applied to Strongly Nonlinear Wave-Body Interaction Problems*, Ph.D. thesis, Norwegian University of Science and Technology (2007).

[16]Matlab, *Version 8.6.0.267246 (R2015b)* (The MathWorks Inc., Natick, Massachusetts, 2015).

[17]M. I. P. Toolbox, *Version 9.3 (R2015b)* (The MathWorks Inc., Natick, Massachusetts, 2015).

[18]J. D'Errico, "Distance based interpolation along a general curve in space," MATLAB Central File Exchange (Retrieved 2014).

[19]D. G. Dommermuth and D. Yue, "Numerical simulation of nonlinear axisymmetric flows with a free surface," J. Fluid Mech. **178**, 195–219 (1986).

[20]F. Fritsch and R. Carlson, "Monotone piecewise cubic interpolation," SIAM Journal on Numerical Analysis **17**, 238–246 (1980).

2. APPENDIX A - ALGORITHMS

2.1. Main Script

```
%clear all
%close all

%uncomment below if using a cluster
%distcomp.feature('LocalUseMpiexec',false)
delete(gcp)
myCluster=parcluster('local')
myCluster.NumWorkers=32
parpool(32)
%%%%%%%%%%%%%%%%%%%%%%%%%%%%%%%%%%%%%%%%%%%%%%%%%%%%%%%%%%%%%%%%%%%%%%%%
%                 User Inputs                                          %
%%%%%%%%%%%%%%%%%%%%%%%%%%%%%%%%%%%%%%%%%%%%%%%%%%%%%%%%%%%%%%%%%%%%%%%%

Frd=71.39;              %Froude Number U^2/Rg
damping=0;
bdy_dx=0.0004;
dx=0.0004;              %node spacing along the water surface
i_l_x=.2;               %interface length in x
i_l_y=1;                %interface length in y (distance to bottom of fluid
                        %domain)
N_d=1000;               %number of nodes on the disk (disk radius = 1)
R_d=.018;               %radius of disk,sphere,or cone
sigma=0.0728;           %surface tension(0.0728 N/m at 20 C for water)
dt=1e-05;               %timestep for Computation, this is the minimum
                        %timestep if using adaptive time stepping
B=127;                  %Bond number
save_interval=10;       %frequency of data file saves
tension=1;              %turns surface tension term on (1) or off (0) in the
```

```
                        %bernoulii equation
sph=0;                  %The shape of the object is a shp=1 is not sph=0
cone=1;                 %The shape is a cone=1 is not cone=0
                        %if sph and cone both =0 a disk is assumed
% bdy_dx=R_d/N_d;
sep_ang=12.5;           %seperation angle of sphere or angle of cone
adaptive_dt=0;          %turn adaptive time step on =1 off=0
dt_max=1e-04;           %max time step that can be acheived in adaptive time
                        %step
t_adjust=2e-05;         %max nodal displacement criteria for adaptive time
                        %step
dt_adapt=1e-06;         %amount to change the time step in adaptive meshing
wag=1;                  %use of wagner's approximation for the shape of the
                        %inital interface

%%%%%%%%%%%%%%%%%%%%%%%%%%%%%%%%%%%%%%%%%%%%%%%%%%%%%%%%%%%%%%%%%%%%%%%%
%                 End User Inputs                     %
%%%%%%%%%%%%%%%%%%%%%%%%%%%%%%%%%%%%%%%%%%%%%%%%%%%%%%%%%%%%%%%%%%%%%%%%

N_i=round((i_l_x/dx)+1);
U_real=sqrt(Frd*R_d*9.81);
U_0=-U_real;
mkdir(['Frd=' num2str(Frd) ', ds=' num2str(dx) ', lx=' num2str(i_l_x)...
    ', tension=' num2str(tension)])

%%%%%%%%%%%%%%%%%%%%%%%%%%%%%%%%%%%%%%%%%%%%%%%%%%%%%%%%%%%%%%%%%%%%%%%%
%          Calculate Initial Domain               %
%%%%%%%%%%%%%%%%%%%%%%%%%%%%%%%%%%%%%%%%%%%%%%%%%%%%%%%%%%%%%%%%%%%%%%%%

x_disk=linspace(0,R_d,N_d);
x_int=(R_d:dx:i_l_x+R_d);
y_disk=zeros(1,length(x_disk))+i_l_y;
```

```
y_int=zeros(1,length(x_int))+i_l_y;
t=0;
if sph>0
    h_sep=R_d-R_d*cos(sep_ang*(pi/180));
    ang_1=3*pi/2;
    srf_ang=(acos((R_d-(h_sep))/R_d));
    num=round(R_d*2*acos((R_d-(h_sep))/R_d)/bdy_dx)+1;
    t_sep=linspace(ang_1,ang_1+srf_ang,num);
    y_disk=i_l_y-h_sep+(R_d*sin(t_sep))+R_d;
    x_disk=R_d*cos(t_sep);
    x_disk(1)=0;
    x_int=(x_disk(end):dx:i_l_x+R_d);
    y_int=zeros(1,length(x_int))+i_l_y;
    N_d=length(x_disk);
    disk_nodes=N_d;
    h_cyl=h_sep;
end
if cone>0
    cone_h=R_d/(tan(sep_ang*(pi/180)));
    cone_side=sqrt(cone_h^2+R_d^2);
    num=round(cone_side/bdy_dx);
    y_disk=linspace(i_l_y-cone_h,i_l_y,num);
    x_disk=linspace(0,R_d,num);
    N_d=length(x_disk);
    disk_nodes=N_d;
    t=0.01438;
    U_0=-(-7.5527*t^2+6.0857*t+3.5516);
end
if wag==1
    dr_ang=90-sep_ang;
    c_dpth=(R_d*2*tan(dr_ang*(pi/180)))/pi;
    y_int=1+((x_int.*c_dpth)./R_d).*asin(R_d./x_int)-c_dpth;
```

```
    y_disk=y_disk+(y_int(1)-1);
    t=0.01438;
end
phi=zeros(1,(length(x_int)-1));
iter=1;
adapt=1;
phi_disk=zeros(1,length(x_disk)-1);
[xb,yb,bt,bv,Nw]=domain (x_disk,x_int,y_disk,y_int,U_0,phi,dx,...
    i_l_x,i_l_y,adapt,phi_disk);
adapt=1;
n = length (xb)-1;% n = number of elements
xm (1:n)=0.5*(xb(1:n)+xb((1:n)+1));
ym (1:n)=0.5*(yb(1:n)+yb((1:n)+1));
xx_new=fliplr(xm(Nw+1:end-N_d+1));
yy_new=fliplr(ym(Nw+1:end-N_d+1));
npt=N_i-1;
dxdt=0;
dydt=0;
dudt_t=0;
m=1;
xsave=save_interval;
pt=1;
% end
stop=1;
u_post=0;
u_post_y=0;
u_post_yproj=0;
vol_post=0;
t_post=0;
r_post=0;
U_proj_post=0;
force_post=0;
```

```
sve_num=0;
phi1=zeros(1,N_d);
while stop>.0001;
    [xb, yb, bt, bv, Nw, adapt]=domain (x_disk,x_int,y_disk,y_int,U_0,...
    phi,dx,i_l_x,i_l_y,adapt,phi_disk);
    n = length (xb)-1;% n = number of elements

    clear lm nx ny nydiv nxdiv
    % Find midpoints and lengths of elements, and their unit normal vectors

    xm (1:n)=0.5*(xb(1:n)+xb((1:n)+1));
    ym (1:n)=0.5*(yb(1:n)+yb((1:n)+1));
    hseg=(sqrt(diff(xm).^2 + diff(ym).^2))';
    [k,nx,ny,tnx,tny]=curvature (xm,ym,N_d,hseg);
    lm(1:n)=((xb((1:n)+1)-xb(1:n)).^2+(yb((1:n)+1)-yb(1:n)).^2).^.5;
    yb1=yb(1:end-1);
    xb1=xb(1:end-1);
    yb2=yb(2:end);
    xb2=xb(2:end);
    ubc=zeros(1,N_d)+U_0;
    if or(sph==1,cone==1)
        nx(end)=-nx(end);
        ny(end)=-ny(end);
        xxx=-(fliplr(U_0.*(ny(end-N_d+2:end))'));
        int_vec=(1:1:length(xxx));
        yyy=interp1(int_vec(2:end),xxx(2:end),int_vec(1),'pchip','extrap');
        if cone==1
            xxx(end)=xxx(end-1);
        end
        bv(end-N_d+2:end)=[yyy;xxx(2:end)];
        ubm=(flipud([yyy;xxx(2:end)]))';
        ubc=interp1(ym(end-N_d+2:end),ubm,y_disk,'pchip','extrap');
```

```
  end

  b=zeros(1,n); %preallocate b
% Boundary Element Method
  parfor m = 1:n

      bb = zeros(1,n);

      [f,g] = influencev (xb1,yb1,xb2,yb2,xm(m),ym(m),m);
      sing=zeros(length(bv),1);
      sing(m)=1;
      zz=find(bt==0);
      zmin=min(zz);
      zmax=max(zz);

      A1(m,:)=g(zmin:zmax)';
      A2(m,:)=-0.5.*sing(zmax+1:n)'-f(zmax+1:n)';
      A3(m,:)=-0.5.*sing(1:zmin-1)'-f(1:zmin-1)';

      bb(zmin:zmax)=bv(zmin:zmax).*(f(zmin:zmax)+0.5.*sing(zmin:zmax));
      bb(1:zmin-1)=bv(1:zmin-1).*-g(1:zmin-1);
      bb(zmax+1:n)=bv(zmax+1:n).*-g(zmax+1:n);
      b(m)=sum(bb);

  end

  % solve system "Ax = b" and store in z
  A=[A3 A1 A2];

  z=gmres(A,b',30,1e-8,30);

  clear phi u x_int y_int F G A b A1 A2 A3
```

```
%     Assign approximate boundary values

phi(1:n)=(1-bt(1:n)).*bv(1:n)+bt(1:n).*z(1:n);
u(1:n)=(1-bt(1:n)).*z(1:n)+bt(1:n).*bv (1:n);

%Extract interface component of domain for computation of new interface
%location and velocity potential

x_marker=fliplr(xb(Nw+1:end)');
y_marker=fliplr(yb(Nw+1:end)');
x_int=x_marker(N_d:end);
y_int=y_marker(N_d:end);
xm=fliplr(xm(Nw+1:end));
ym=fliplr(ym(Nw+1:end));
phin=fliplr(phi(Nw+1:end));
el=fliplr(lm(Nw+1:end));
un=fliplr(u(Nw+1:end));
nx=fliplr(nx(Nw+1:end));
ny=fliplr(ny(Nw+1:end));
phi_disk=interp1(xm(1:N_d-1),phin(1:N_d-1),x_marker(1:N_d),...
    'pchip','extrap');
u_disk=zeros(1,length(phi_disk))+U_0;
tm=[x_int(1) cumsum(sqrt(diff([x_int(1) xm(N_d:end)]).^2+...
    diff([y_int(1) ym(N_d:end)]).^2))];
t_new=[x_int(1) (cumsum(sqrt(diff(x_int).^2+diff(y_int).^2)))];
u=interp1(tm(2:end),un(N_d:end),t_new);
u(1)=U_0;
u(end)=0;
phi=interp1(tm(2:end),phin(N_d:end),t_new);
phi(1)=phi_disk(end);
phi(end)=0;
```

```
clear d_q

[d_q,x,y,x_disk,y_disk,dt,force,phi1]=potential(x_marker,y_marker,...
    [phi_disk phi(2:end)],[u_disk u(2:end)],Frd,B,N_d,dt,nx,ny,...
    adapt,damping,i_l_y,R_d,sigma,tension,sph,ubc,sep_ang,dx,...
    adaptive_dt,dt_max,t_adjust,dt_adapt,phi1,bdy_dx);
nosplx=x;
nosply=y;

clear xx_new yy_new

% adapt mesh and velocity potential for next timestep

[x_disk,y_disk,phi,npt,x_int,y_int,xx_new,yy_new,pt,stop]  =...
    adaptive_mesh(x,y,N_d,dt,x_int,y_int,i_l_x,d_q,dx,npt,...
    bv,xb,yb,U_0,Nw,x_disk,y_disk,adapt,phi_disk,R_d,sph,cone,2e-04);

iter=iter+1;
t=(t+dt)
%comment below for a constant velocity
U_0=-(-7.5527*t^2+6.0857*t+3.5516);

if xsave==save_interval
    sve_num=sve_num+1;
    xsave=0;
    cd(['Frd=' num2str(Frd) ', ds=' num2str(dx)...
        ', lx=' num2str(i_l_x) ', tension=' num2str(tension)])
    save([num2str(sve_num) '.mat'])
    cd ..
end
xsave=xsave+1;
```

```
end
cd(['Frd=' num2str(Frd) ', ds=' num2str(dx) ', lx=' num2str(i_l_x)...
    ', tension=' num2str(tension)])
save('final.mat')
cd ..

parpool('close')
```

2.2. Functions

```
function [xb yb bt bv Nw, adapt]=domain (x_disk,x_int,y_disk,y_int,U_0,...
    phi,dx,i_l_x,i_l_y,adapt,phi_disk)

%Construct interface, and far field boundaries

x_interface=[x_disk x_int(2:end)];
y_interface=[y_disk y_int(2:end)];
 x_bottom=linspace(0,x_interface(1,end),(x_interface(1,end))/(dx*10));
y_bottom=zeros(1,length(x_bottom));

N_right=i_l_y/(dx*10);
y_right=linspace(y_interface(1,end),y_bottom(1,end),N_right);
x_right=zeros(1,length(y_right))+x_bottom(1,end);

%assemble boundary vectors and assign boundary conditions

xb=[(x_bottom) fliplr(x_right(2:end-1)) fliplr(x_interface)]';
yb=[(y_bottom) fliplr(y_right(2:end-1)) fliplr(y_interface)]';
bt=[ones(1,length(x_right(2:end))+length(x_bottom)-1)...
    zeros(1,length(x_int(2:end))) ones(1,length(x_disk)-1)]';
bv=[zeros(1,length(x_right(2:end))+length(x_bottom)-1) fliplr(phi)...
    zeros(1,length(x_disk)-1)+(U_0)]';
```

```
if adapt==1
    adapt=2;
else
    adapt=1;
end
%Length of the far field boundary vector
Nw=length(x_bottom)+length(x_right(2:end-1));


function [k,nx,ny,tnx,tny]=curvature (x,y,N_d,h)

[dxdt d2xdt2 dydt d2ydt2] = spl (x,y,h);
%compute element length, arc length, and unit normals (VECTORIZE THIS SAM!)

k=zeros(1,length(x));
R1=(((d2xdt2.*dydt)-(d2ydt2.*dxdt))./(dxdt.^2+dydt.^2).^(3/2));
R2=(-(dydt)./(x.*((dxdt.^2+dydt.^2)).^0.5));

%k=mean curvature
k(2:end-1)=R1(2:end-1)+R2(2:end-1);
k(1:N_d)=0;
norm=sqrt(dxdt.^2+dydt.^2);
nx=zeros(1,length(x));
ny=ones(1,length(x));
tnx=ones(1,length(x));
tny=zeros(1,length(x));
%unit normal and tangent vectors
ny(2:end-1)=dxdt(2:end-1)./norm(2:end-1);
nx(2:end-1)=-(dydt(2:end-1)./norm(2:end-1));
tny(2:end-1)=(dydt(2:end-1)./norm(2:end-1));
tnx(2:end-1)=dxdt(2:end-1)./norm(2:end-1);


end
```

```
function [dxdt d2xdt2 dydt d2ydt2] = spl (x,y,h)

h1=-h(1:end-1)';
h2=h(2:end)';
h21=h2-h1;
dxdt=zeros(1,length(x));
d2xdt2=zeros(1,length(x));
dydt=zeros(1,length(x));
d2ydt2=zeros(1,length(x));

x1=x((2:length(x)-1)-1);
y1=y((2:length(x)-1)-1);
x0=x(2:length(x)-1);
y0=y(2:length(x)-1);
x2=x((2:length(x)-1)+1);
y2=y((2:length(x)-1)+1);
dxdt(2:length(x)-1)=((x2-x0)./h2-(((x2-x0)./h2-(x1-x0)./h1)./h21).*h2);
d2xdt2(2:length(x)-1)=2.*(((x2-x0)./h2-(x1-x0)./h1)./h21);
dydt(2:length(x)-1)=((y2-y0)./h2-(((y2-y0)./h2-(y1-y0)./h1)./h21).*h2);
d2ydt2(2:length(x)-1)=2.*(((y2-y0)./h2-(y1-y0)./h1)./h21);



end

function [F,G] = influencev (x1,y1,x2,y2,x0,y0,m)

xm=(1/2).*(x2+x1);
xd=(1/2).*(x2-x1);
ym=(1/2).*(y2+y1);
yd=(1/2).*(y2-y1);
dr=sqrt(xd.^2+yd.^2);
```

```
nx=yd./dr;
ny=-xd./dr;
%gauss quadriture points
zz=[-0.993128599185095 -0.963971927277914 -0.912234428251326 -0.839116971822219 -0.74633
ww=[0.017614007139152 0.040601429800387 0.062672048334109 0.083276741576705 0.1019301198

x=bsxfun(@plus,xm,(bsxfun(@times,xd,(repmat(zz,length(xm),1)))));
y=bsxfun(@plus,ym,(bsxfun(@times,yd,(repmat(zz,length(ym),1)))));

x0=repmat(x0,length(xm),1);
y0=repmat(y0,length(ym),1);

[G,dGdx,dGdy]= freespacev(x,y,x0,y0);


dd=(y(m,:)-y0(m)).^2+(x(m,:)-x0(m)).^2;
G(m,:)=G(m,:)+log(dd)./(4*pi);


G=sum(bsxfun(@times,dr,(G.*x.*repmat(ww,length(ym),1))),2);
F=sum(bsxfun(@times,dr,(bsxfun(@times,ny,dGdx)+bsxfun(@times,nx,dGdy)).*x.*repmat(ww,len


G(m)=G(m)-2*dr(m)*(log(dr(m))-1)/(2*pi);

end

function [G,dGdx,dGdy] = freespacev (x,y,x0,y0)
dy=bsxfun(@minus,y,y0);
s=(bsxfun(@plus,x,x0)).^2;
rks=4.*(bsxfun(@times,x0,x))./(dy.^2+s);
elliptic_tolerence=1e-16;
```

```
[F, E]=cellfun(@ellipke,mat2cell(rks,ones(1,length(rks))),...
    mat2cell(repmat(elliptic_tolerence,length(rks),1),...
    ones(1,length(rks))),'UniformOutput', false);
F=cell2mat(F);
E=cell2mat(E);
G=(4.*F./(sqrt(dy.^2+s)))./(4*pi);
dGdx=-dy.*((4./(sqrt(dy.^2+s)).^3).*(E./(1-rks)));
dGdy=-x.*((4./(sqrt(dy.^2+s)).^3).*(E./(1-rks)))+...
    (bsxfun(@times,x0,((4./(sqrt(dy.^2+s)).^3).*...
    ((-2.*F+(2-rks).*E./(1-rks))./rks))));
dGdx=dGdx./(4*pi);
dGdy=dGdy./(4*pi);
end

function [d_q,x,y,x_disk,y_disk,dt,force,phi1]=potential(xm,ym,phi,u,...
    Frd,B,N_d,dt,nx,ny,adapt,damping,i_l_y,R_d,sigma,tension,...
    sph,ubc,sep_ang,dx,adaptive_dt,dt_max,t_adjust,dt_adapt,phi1,bdy_dx)

%Extract the interface nodes and disk edge node
phi=phi-(dt.*damping.*phi);
x=xm;
y=ym;
if adapt==2
    [phi1,force]=cone_force(phi,phi1,nx,ny,dt,u,x,y,N_d,i_l_y,...
        bdy_dx,sigma,sep_ang,R_d);
    else
    force=0;
end
n=length(xm);
step=dt;
X1=[phi',x',y'];
[fphi1,fx1,fy1] = potential_update (X1,n,u,Frd,B,nx,ny,N_d,damping,...
```

```
    step,i_l_y,R_d,sigma,tension,sph,ubc,sep_ang,dx);
d_q=phi+(fphi1.*step);
x=x+(fx1.*step);
x=[xm(1:N_d) x(N_d+1:end)];
y=y+(fy1.*step);
y=[ym(1:N_d)+u(1:N_d).*step y(N_d+1:end)];
if adaptive_dt==1
    d_chk=max(((x(N_d+1:end)-xm(N_d+1:end)).^2+(y(N_d+1:end)-...
        ym(N_d+1:end)).^2).^.5);
    if d_chk > t_adjust && (dt-dt_adapt)~=0
        dt=dt-dt_adapt;
    end
    if d_chk < t_adjust && dt < dt_max
        dt=dt+dt_adapt;
    end
end
x_disk=x(1:N_d);
y_disk=y(1:N_d);

if sph>0
    [x,y,x_disk,y_disk]= sphere_pen_check (sep_ang,N_d,R_d,x,y,dx);
end
%remove excessive splash/jetting at surface
hseg=arclength(x,y,'pchip');
[k,~,~,~,~]=curvature (x,y,N_d,hseg);
[~,b]=find(y>1);
[~,d]=max(x(N_d:b(1)));
[~,f]=min(x(b));
[~,h]=max(k);
if (x(N_d+d)-x(b(1)+f))>1e-03
    x=[x(1:h-2) x(h+2:end)];
    y=[y(1:h-2) y(h+2:end)];
```

```
    d_q=[d_q(1:h-2) d_q(h+2:end)];
end
end

function [phi1,force]=cone_force(phi,phi1,nx,ny,dt,u,x,y,N_d,i_l_y,...
    bdy_dx,sigma,sep_ang,R_d)

%note this code uses a constant polar angle and normal velocity on the
%surface it will need to be modified for other shapes.
phi2=phi(1:N_d);
roh=998.2071;
hseg=arclength(x,y,'pchip');
[t_phi] = tangen_vel(phi,x,hseg);
[~,nx,ny,~,~]=curvature (x,y,N_d,hseg);
ny(1)=ny(2);
ny(N_d)=ny(N_d-1);
nx(1)=nx(2);
nx(N_d)=nx(N_d-1);
fx=(t_phi(1:N_d).*ny(1:N_d))+(u(1).*nx(1:N_d));
fy=(-t_phi(1:N_d).*nx(1:N_d))+(u(1).*ny(1:N_d));

dphidt=((phi1-phi2)./dt)-(((u(1)*nx(1)).*(fx))+((u(1)*ny(1)).*(fy)));

s=[0 cumsum(hseg(1:N_d-1))'];
cone_height=y(2:N_d)-y(1:N_d-1);
cone_area=pi.*(x(2:N_d)+x(1:N_d-1)).*sqrt((x(2:N_d)-x(1:N_d-1)).^2+...
    cone_height.^2);

intg=(dphidt-(0.5.*(t_phi(1:N_d).^2))-(9.81.*(y(1:N_d)-(i_l_y))));

polar_angle=((sep_ang)*(pi/180));
edge_angle=(pi/2)-atan2(y(N_d+1)-y(N_d),x(N_d+1)-R_d);
```

```
force=sum(cone_area)*roh*((0.5*(u(1)*ny(2))^2)-(polar_angle*...
    trapz(s,intg))+((2*sigma*cos(edge_angle))/(roh*R_d)));
phi1=phi2;
end

function [fphi, fx, fy] = potential_update (X,n,u,Frd,B,nx,ny,N_d,damping,dt,i_l_y,R_d,s
phi_i=X(:,1)';
x=X(:,2)';
y=X(:,3)';
hseg=(sqrt(diff(xm).^2 + diff(ym).^2))';
h=(cumsum(hseg))';
[k,nx,ny,tnx,tny]=curvature (x,y,N_d,hseg);
if sph==1
    k(1:N_d)=-(1/R_d);
end
u(1:N_d)=ubc;
[t_phi] = tangen_vel(phi_i,x,hseg);
fx=(t_phi.*ny)+(u.*nx);
fy=(-t_phi.*nx)+(u.*ny);
if tension==1
    fphi=(1/2).*(t_phi.^2+(u).^2)-((sigma.*k)./998.2071)-(9.81.*(y-(i_l_y)));
else
    fphi=(1/2).*(t_phi.^2+(u).^2)-9.81.*(y-(i_l_y));
end
end

function [x_disk,y_disk,phi,npt,x_int,y_int,xx_new,yy_new,pt,stop] =...
    adaptive_mesh (x,y,N_d,dt,x_int,y_int,i_l_x,d_q,dx,npt,...
    bv,xb,yb,U_0,Nw,x_disk,y_disk,adapt,phi_disk,R_d,sph,cone,dx_cav)
xm=x;
ym=y;
while round(x(1,end)*100)*.01==i_l_x+R_d
```

```
    x=x(1:end-1);
    y=y(1:end-1);
end

px=x(N_d:end);
py=y(N_d:end);

%Interparc is a script by John D'Errico (see references)
[pt]=interparc(npt*4,px,py,'pchip');

N_d=N_d+1;
stop=min(pt(:,1));
clear dudt t

xb_new=pt(1:2:end,1)';
yb_new=pt(1:2:end,2)';

xx_new=pt(2:2:end,1)';
yy_new=pt(2:2:end,2)';

if length(xb_new)==length(xx_new)
    xb_new(1,end+1)=xb_new(1,end)+((xb_new(end)-xb_new(end-1))^2+...
        (yb_new(end)-yb_new(end-1))^2)^.5;
    yb_new(1,end+1)=yb_new(1,end);
end

if adapt==2
    x_int=[xb_new(1) xb_new(2:2:end)];
    y_int=[yb_new(1) yb_new(2:2:end)];
    xx_new=[xx_new(1) xb_new(3:2:end-1)];
    yy_new=[yy_new(1) yb_new(3:2:end-1)];
else
```

```
    x_int=xb_new(1:2:end);
    y_int=yb_new(1:2:end);
    xx_new=xb_new(2:2:end-1);
    yy_new=yb_new(2:2:end-1);
end
if x_int(1,end)>i_l_x+1
    x_int=x_int(1:end-1);
    y_int=y_int(1:end-1);
    xx_new=xx_new(1:end-1);
    yy_new=yy_new(1:end-1);
end
tm=[0 (cumsum(sqrt(diff(xm).^2+diff(ym).^2)))];
t_new=[0 cumsum(sqrt(diff([xm(1:N_d-1) xx_new]).^2+diff([ym(1:N_d-1)...
    yy_new]).^2))];
phi=interp1(tm,d_q,t_new(N_d:end),'pchip','extrap');

l(1:length(xx_new)-1)=sqrt((xx_new((1:length(xx_new)-1)+1)-...
    xx_new(1:length(xx_new)-1)).^2+(yy_new((1:length(xx_new)-1)+1)-...
    yy_new(1:length(xx_new)-1)).^2);

if max(abs(l))>dx
    npt=npt+1;
end
if sph==0 && cone==0
    y_disk(1:end)=y_int(1,1);
end
end
```